Stucki and Maynes
Advances in Aerodynamics (2022) 4:37
https://doi.org/10.1186/s42774-022-00131-z

Advances in Aerodynamics

RESEARCH Open Access

Drag reducing nose fairings for existing freight train locomotives

Chad L. Stucki[1] and Daniel Maynes[2*]

*Correspondence: maynes@byu.edu

[1] Corvid Technologies, Mooresville, NC 28115, USA
[2] Department of Mechanical Engineering, Brigham Young University, Provo, UT 84602, USA

Abstract

At cruising speed, one of the most significant contributing factors to train fuel consumption is aerodynamic drag, and the leading locomotive experiences much more drag than any other car in the train. This work reports on the drag reduction that can be realized by the use of add-on nose fairings that are deployed on leading locomotives in a train set. Two types of fairing shapes were considered and all fairing walls are flat. It is anticipated that the fairing shapes would result from the deployment of easily stowed panels in an origami inspired manner. One of the fairing shapes has the appearance of a wedge and the other fairing is also wedge shaped, but with flow directing side wall features. For each general fairing shape, the important dimensions were parametrically varied in a systematic manner to identify the dimensions that yield maximum drag reduction. For the first shape, 45 different scenarios were considered; for the second shape, 15 were considered. A steady commercial computational fluid dynamic solver was employed to solve the flow field and locomotive drag for each of the scenarios. The best performing wedge-shaped fairing reduced the leading locomotive drag by nominally 14% and the best performing fairing shape with the side walls reduced the drag by 17%.

Keywords: Drag reduction, Front-fairing, Origami, Locomotive

1 Introduction

Transportation of goods by rail continues to be a vital component of the United States freight distribution system. In 2011, the U.S. railroad and trucking industries moved 1729 and 2644 billion ton-miles of freight, respectively, and the total annual fuel consumption for each industry was respectively, 3.7 and 28.2 billion gallons of diesel fuel [1]. Fuel requirements for freight trains are directly related to their tractive resistance, and at cruising speed aerodynamic drag is a significant contributor to the overall tractive resistance [2–4]. Further, the first locomotive in a train experiences significantly higher aerodynamic drag than subsequent cars [2]. The total resistance is comprised of rolling or sliding friction between train wheels and rails, friction that prevails on rotating shafts and bearings, and aerodynamic drag. At steady speed the total tractive force must overcome the combined resistances. There has been much recent research related to improving the fuel efficiency and understanding the overall performance of train systems [5].

The total aerodynamic drag is a combination of skin friction drag and pressure drag. Freight locomotives are non-streamlined bluff-body shapes with many protuberances and discontinuities. Thus, the flow field around them is turbulent and dominated by regions of flow separation. Consequently, pressure drag is the largest contributor to the aerodynamic drag, and the locomotive drag coefficient is largely independent of the Reynolds number [2, 6, 7]. Golovanevskiy et al. provide guidelines for the length required for both CFD modeling and wind tunnel testing of train sets with streamlined locomotives to determine: 1) the drag on the leading locomotive; and 2) the near constant drag on the intermediate cars in the train set. They show that the drag on the leading locomotive becomes independent of the number of cars behind it if the total number of cars/locomotives is more than five [2]. Even fewer cars are needed if the locomotives are non-streamlines, such as freight locomotives. Golovanevskiy et al. also reported that drag coefficient independence for freight trains and railcars occurs at Reynolds numbers (based on locomotive width) as low as 6×10^5 [2]. Pressure drag is especially high on the leading locomotive, and trains with more railcars exhibit less drag on a per car basis. As a result, freight trains are often composed of as many as 200 railcars or more [2]. Thus, aerodynamic modifications rendered to every railcar are more effective at reducing the overall aerodynamic drag than modifications exclusive to the lead car. However, a single modification made to the lead locomotive has greater drag reducing potential than a single modification made to a single railcar in the middle of a train.

Several prior investigators have focused on modifications to the cars of freight trains to decrease their drag. Watkins et al. performed wind tunnel tests on 1/10th scale hopper and gondola cars [8]. They showed that by attaching covers the drag on unfilled cars decreased by approximately 25%. Condie and Maynes similarly explored attaching covers to coal carrying cars and showed drag reductions on individual cars of a similar amount [9]. Condie also considered modifications to auto-carrying railcars and identified three regions that contribute significantly to the aerodynamic drag: the roof, side panels, and underbody. In the baseline model, the roof was characterized by corrugations oriented perpendicular to the free stream flow, the side panels were patterned with holes for ventilating exhaust, and wheel assemblies and other mechanical systems occupied the space beneath the undercarriage. To minimize the drag penalties from each device, Condie attached smooth covers to the roof, replaced the side panels with panels consisting of a variety of hole and slot patterns, and installed covers and skirts for streamlining the underbody. Ultimately, the best roof, side panel, and underbody modifications predicted 20%, 5%, and 15% drag savings, respectively. Kinghorn performed wind tunnel tests on articulated well car sets loaded with intermodal containers to identify drag penalties associated with leaving some wells empty [10] and Lai and Barkan employed wind tunnel data and a computational tool to explore strategies for more effective loading of intermodal cars [11]. They showed the overall tractive resistance of a train could be reduced by as much as 27% when voids in loading of intermodal containers are eliminated.

There have been many prior studies aimed at decreasing drag and improving efficiency of semi-truck tractors and trailers. The flow around heavy trucks and trailers is unsteady, three dimensional, and due to the boxy shape and many sharp corners is dominated by flow separation and correspondingly high drag. Attention has been given to

forebody drag (tractor), base drag (due to flow separation on the rear of the trailer), and underbody drag [12]. Much work has focused on the implementation of cab fairings on tractor-trailer combinations [13–16]. These fairings act to minimize drag by preventing air from stagnating on the front of the trailer. Chowdhury et al. performed wind tunnel tests on a 1/10th scale model truck to determine the drag-reducing potential for two such add-on cab fairings [17]. The first was a fairing with gap extenders, and the second was a fairing without. The gap extenders acted to fill the tractor-trailer gap. Their results showed that the overall drag on the tractor-trailer combination was reduced by 18% and 26%, respectively, when the two fairings were added. Base drag reduction methods have also been explored by implementing roof rounding, rear flaps, vortex generators, and boat tail shapes. Much less attention has been devoted to underbody drag, although the implementation of side flaps is widely adopted [12].

In contrast to heavy road vehicles or freight trains, high speed trains may operate at speeds in excess of 180 mph, more than three times faster than a typical freight train [12]. Consequently, they are highly streamlined and flow separation effects and pressure drag represent a much smaller portion of the overall drag, compared to freight trains where pressure drag is dominant. While drag reduction is important for high speed trains, pressure waves in tunnels, dynamics associated with two trains passing, impacts of crosswind and aerodynamic noise are also important issues that arise from the elevated speed and that have received significant attention in the literature [18, 19].

There have been significant prior efforts to explore drag reduction by streamlining passenger trains and engines, and all modern high-speed trains employ streamlined engines [20–23]. Kwak et al. performed an optimization using CFD to improve the geometry of a high-speed passenger train [24]. They considered aerodynamic effects at both ends of the train, modeling the entire length of the train. They showed that their optimized geometry could provide a 23% drag reduction compared to a baseline geometry from a study which only considered effects at the front end. Li et al. conducted detached eddy simulations to explore the flow around high speed trains with different nose lengths [25]. Here both the leading and trailing cars had extended noses that ranged in length from 4 to 12 m. They explored impacts of the nose length on the drag and lift forces experienced by the leading and trailing cars, the generated slipstream velocity due to train passing, and the instantaneous wake of the train. Their result showed that by increasing the length of the fairing from 4 m to 7 m, the drag on the leading car decreased by 17.6% and the drag on the trailing car decreased by 29.3%. Others have also implemented numerical modeling to investigate effects of nose geometry on slipstream velocities [26], drag reduction caused by implementation of pantograph fairings [27], and the combined effect of nose shape and yaw on flow structures [28].

Relative to high speed passenger trains, freight trains travel at relatively low speeds and aerodynamic drag is a smaller contributor to the overall tractive resistance. Consequently, there have been few studies that have explored the benefit of streamlined locomotives for freight trains. Thus, freight trains have less streamlined profiles that are more disruptive to the flow and yield larger wakes than passenger trains. Nevertheless, some initial studies on freight train locomotives have been performed. For example, Iden conceptualized an array of frontal vanes, a set of rear fairings, and a pair of radiator fairings for freight locomotive use [29]. Importantly, there are very few archived studies that

have explored the impact of fairing use on the drag reduction of freight locomotives, even though their implementation has resulted in notable drag reduction for both very streamlined high speed trains and for bluff body style vehicles. Thus, there is a significant motivation to explore this scenario.

Origami inspired design has been utilized for many engineering scenarios where a combination of folded panels can morph from a compact volume in a stowed position to a functional shape when the panels are deployed [30–32]. Tolman et al. reported on the design of a deployable locomotive fairing utilizing origami principles [33]. The focus of this paper is to report on results from a Computational Fluid Dynamic (CFD) study exploring the influence on locomotive drag that origami-inspired add-on fairings can yield to existing freight train locomotives. This work was performed in conjunction with the design work of Tolman et al. [33]. The work explores two fairing shapes. Within each general shape, a population of many fairing geometries is explored and a best performing geometry is identified from each shape class. The goal is to explore a very large number of flat panel configurations to identify design rules to guide implementation of a simple and low-cost fairing that can be deployed on an existing train fleet. There have been few prior studies that address the impact of add-on fairings to existing freight locomotives, and no prior studies that have considered the origami style flat panel fairings described here. Thus, the present work fills an important hole in the literature related to fairing implementation for reducing drag on freight locomotives, and in particular for fairings that could be built and deployed using the flat panel requirements of origami inspired design.

The remainder of this paper is laid out in the following manner. First, the real-world constraints on the fairing shape dimensions will be presented, and the two general fairing shapes will be described in terms of the important design parameters. Subsequently, the CFD approach will be reviewed and this will be followed by a discussion of the qualitative and quantitative CFD results. Finally, conclusions from the work will be presented.

2 Methodology

2.1 Constraints

In a train set, freight locomotives may be positioned and oriented in a variety of ways. They may be forward-facing, rear-facing, coupled to the front of the train, to the back of the train, or between two railcars. However, the majority of them will lead the train at some point in time. Clearly, these coupling requirements must be satisfied when add-on nose fairings are attached. Some of these requirements constrain the fairing differently when it is attached to a non-lead locomotive than when it is attached to the lead locomotive. For example, when two locomotives are joined in a nose-to-nose fashion, the amount of space available for the two fairings is very limited. In contrast, lead locomotives offer a significant amount of space for the fairing. The space available to fairings for each configuration is illustrated by the gray shaded regions in Fig. 1. The need for headlights, windshields, snow plows, and walkways to serve their functions also constrains the available space. Each of these devices is labeled in the figure. Note that the walkways span a width of 61 cm. Furthermore, the 6-degree taper shown in the lower right of Fig. 1 allows coupled locomotives to turn along curved tracks without interference between the two fairings. Although the headlights and

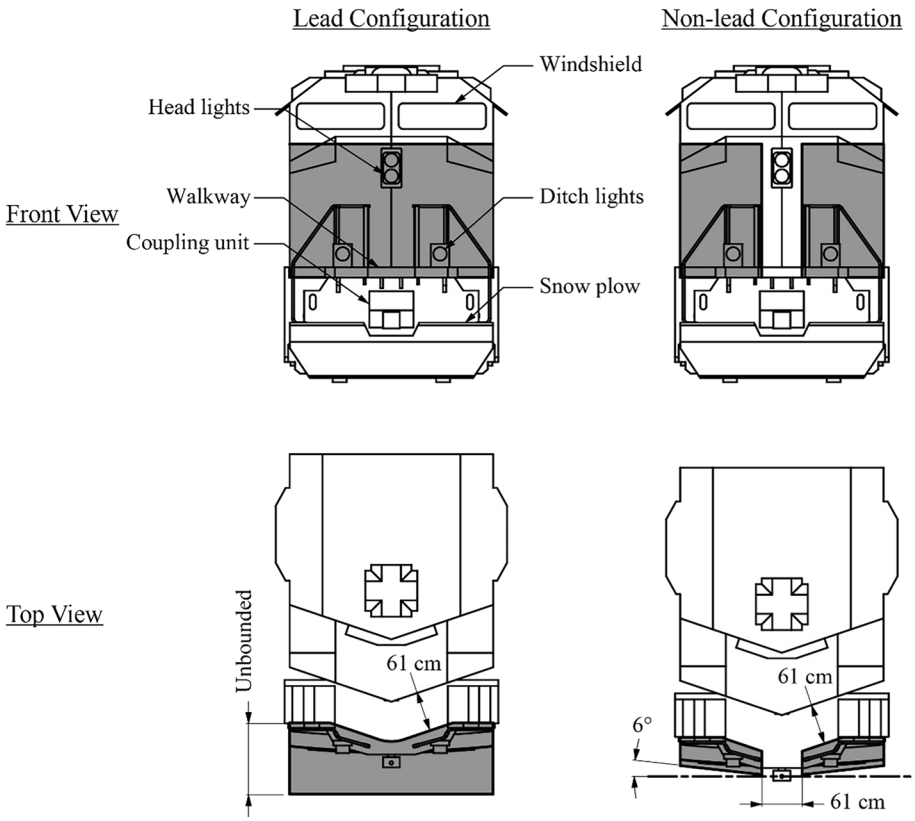

Fig. 1 Front and side views of a typical freight train locomotive. The gray regions in this figure highlight the space that is available for an add-on nose fairing. Due to the different spatial requirements for lead (left) and non-lead (right) locomotives, the available space is shown for both configurations. A top view and a front view are provided for each configuration. Devices on the locomotive that constrain the available space for the fairing are appropriately labeled

ditch lights must illuminate the path and objects ahead of the lead locomotive and be visible to neighboring and oncoming traffic, it is assumed that transparent windows may be used. Thus, the headlights and ditch lights may still serve their functions when the fairings occupy the spaces shown.

2.2 Primary fairing shape

Due to the confined space between coupled locomotives, an origami construction as described by Tolman et al. was conceptualized for fairing design [33]. Thus, the fairing may be deployed on the lead locomotive and folded into a stowed position for non-lead locomotives. Such a concept requires the fairing to consist of flat and foldable panels. Furthermore, ease of use and a low-cost manufacture require the fairing to consist of as few panels as possible.

This work focuses on two origami families of fairing shape, and are denoted here as the primary and secondary shapes. As stated in the introduction, the primary shape has the appearance of a wedge. Three design variables were selected to define the primary fairing shape; namely, fairing length (x_{1A}), tip height (x_{2A}), and tip width (x_{3A}). These variables are shown in Fig. 2. Each geometry obeys the following design parameter bounds:

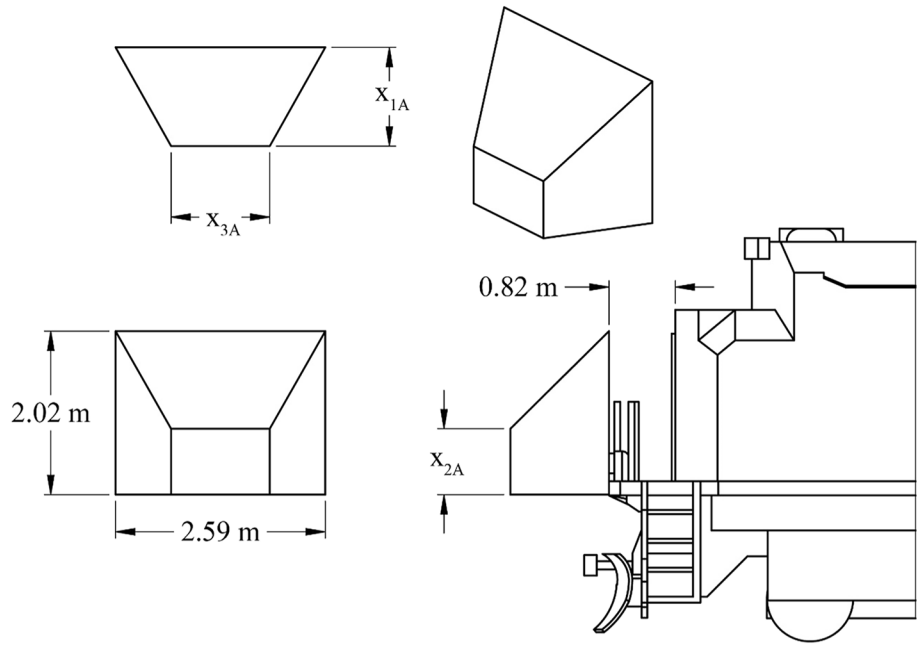

Fig. 2 Top, front, side, and isometric views for the primary fairing shape. The shape is governed by three parametric design variables: fairing length (x_{1A}), tip height (x_{2A}), and tip width (x_{3A}). The overall fairing width, height, and the gap between the fairing and locomotive remain constant from one fairing geometry to the next

$$61 \leq x_{1A} \leq 183 \text{ [cm]}, \tag{1}$$

$$0 \leq x_{2A} \leq 183 \text{ [cm]}, \tag{2}$$

$$61 \leq x_{3A} \leq 244 \text{ [cm]}. \tag{3}$$

For the most part, the aforementioned spatial constraints governed the bounds for each of the three design variables. Nevertheless, the bounds were also selected based on what was believed to perform well at reducing the aerodynamic drag. For example, it was believed that the side fairing panels should deflect the air outwards. Thus, the upper bounds for x_{2A} and x_{3A} were less than the overall fairing width. Note that the overall fairing height (202 cm), width (259 cm), and the gap between the fairing and locomotive (82 cm) remained fixed as the fairing changed shape. Collectively, the fairing length and tip height govern the slope of the top panel. Too great a value of tip height (x_{2A}) could cause the top panel to direct the oncoming airflow into the windshield. As a result, the linear constraint,

$$0 \leq x_{2A} \leq -0.32\, x_{1A} + 202 \text{ [cm]} \tag{4}$$

was assigned to maintain the tip height at a value to satisfy this constraint. Finally, based on intuition, it was believed that a very long fairing could not sustain the resulting aerodynamic loads, so a 183-cm maximum was set on x_{1A}. Within the bounded space, a structured array of 45 primary fairing geometries was produced.

2.3 Secondary fairing shape

In addition to the fairing geometries discussed in this paper, Stucki et al. explored over 200 other shapes [34]. They found that the addition of a side wall feature yielded an appreciably greater reduction to the aerodynamic drag. As a result, this paper presents a secondary fairing shape in which the side wall feature is added to a singular geometry from the primary fairing shape. Each of the geometries of the secondary shape is assigned the fixed values $x_{1A} = 74$ cm, $x_{2A} = 0$ cm, and $x_{3A} = 191$ cm. However, the side wall feature height, x_{1B}, varies discreetly between the following bounds:

$$0 \leq x_{1B} \leq 38 \text{ [cm]}. \tag{5}$$

The side wall height is defined as shown in Fig. 3. As demonstrated in the results, the last few increments in side wall height showed no further reductions to the aerodynamic drag. As a result, no greater values of side wall height were explored. The secondary fairing shape consisted of fifteen geometries, and a CFD model was used to predict the drag performance for all 60 geometries from the primary and secondary fairing shapes.

2.4 Computational model

Shown in Fig. 4 are front and side views of the computational domain and locomotive configuration employed for this study. For all scenarios considered, two locomotives were included in the CFD model. Additional downstream cars from the second locomotive were not included to provide computational efficiency. Additional downstream cars would alter only modestly the drag on the leading locomotive and neglecting them is justified since the goal of the work is to identify relative reductions in drag on the leading locomotive due to add on fairings. The domain extended

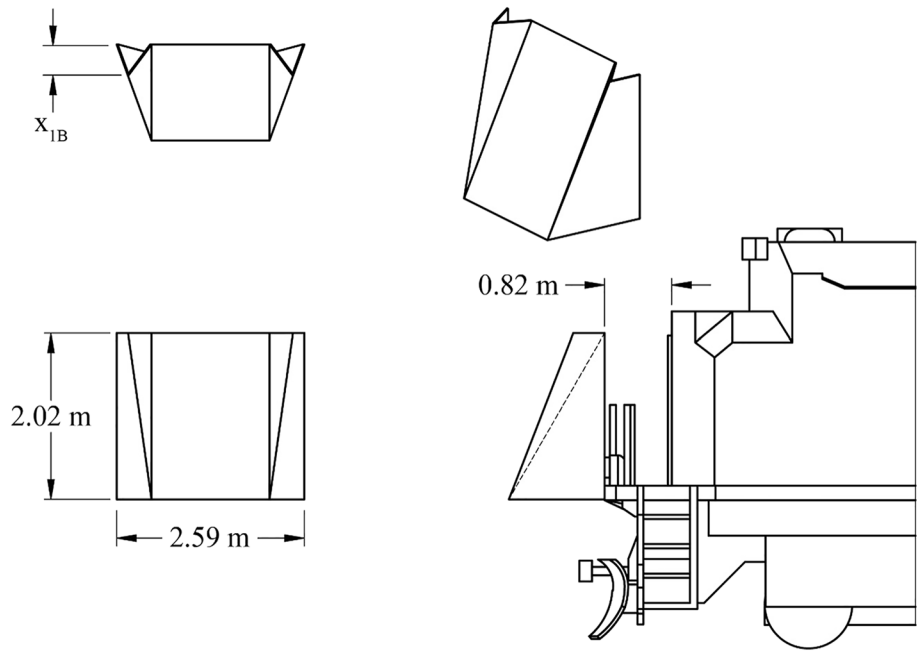

Fig. 3 Top, front, side, and isometric views for the secondary fairing shape. The shape is governed by one parametric design variable: fairing side wall depth (x_{1B}). The overall fairing width, height, and the gap between the fairing and locomotive remain constant from one fairing geometry to the next

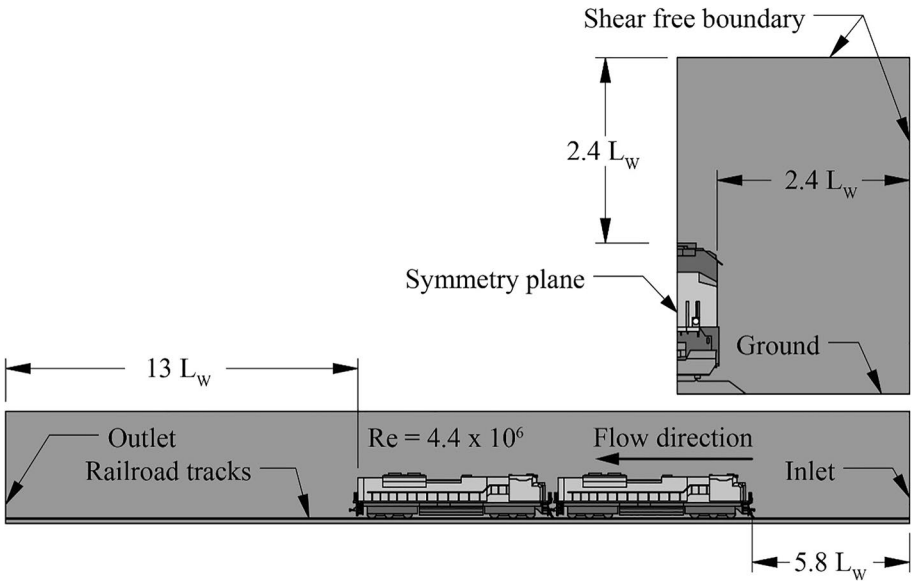

Fig. 4 Illustration of computational domain size and description of boundary conditions

nearly six locomotive widths in front of the train set, 13 locomotive widths behind the trailing locomotive, and nominally 2.5 locomotive widths above and to the side. Minor asymmetry exists in production locomotives, however here the computational domain and locomotive were modelled as symmetric. Thus, the left plane of the domain was modeled as a symmetry plane. A uniform velocity was prescribed at the domain inlet and this same velocity was applied to the railroad tracks, subgrade, and ground as a translating boundary condition to simulate motion between the locomotives and ground. Shear-free boundaries were specified at the top and side boundaries, and a pressure outlet condition was specified at the outlet of the domain. Based on a locomotive width (L_w) of 3 m and a freestream velocity (U_∞) of 22.4 m/s, the Reynolds number ($U_\infty L_w/\nu$) was nominally 4.4×10^6 for all simulations, where ν is the kinematic viscosity.

The simulations were performed using CD-ADAPCO's Star-CCM+ code. The wall-normal size of the cells on the surfaces is in the $30 < y+ < 50$ range. A polyhedral volume mesh was accompanied by six prism layers at the locomotive and computational floor boundaries. The total number of cells for all scenarios considered varied between 3.5 and 4 million. The primary goal of the study was to provide a rapid assessment of the relative changes in the drag on a locomotive due to the addition of the 200 unique fairings considered (results for 60 included here). A comprehensive grid refinement study was thus not performed. Instead, the computational grid refinement was maintained to be identical for all scenarios considered, with the only variation being the grid around the changing fairing geometries that were attached for the different cases. In this manner, the relative changes between the overall drag for each of the 200 simulations could be compared in a timely manner and all at the same level of CFD accuracy.

A steady segregated incompressible flow solver was employed with velocity and pressure under-relaxation factors of 0.7 and 0.3, respectively. Fluid properties were

specified as air at standard conditions. Turbulence was modeled using the realizable k-ε RANS model with the second order convection scheme employed. Two-layer all $y+$ wall functions were utilized to resolve the boundary layer. Constant parameters in the k-ε model were set at the following parameters [35]: $C_\mu = 0.09$, $\sigma_k = 1.0$, $\sigma_\epsilon = 1.2$, $C_{1\epsilon} = 1.44$, and $C_{2\epsilon} = 1.9$. In order to ensure convergence, an asymptotic criterion was used to shut down the solver. Convergence was specified when the drag on the leading locomotive varied by less than 0.025% over the course of 200 iterations.

2.5 Wind tunnel validation

A limited set of wind tunnel tests were also performed. The tests were conducted in a wind tunnel with a test section of 1.22 m in width, 0.61 m in height and 5.1 m in length. We summarize the experimental process here, but a detailed description is given by Condie and Maynes [9] and Kinghorn [10]. The wind tunnel is an open concept tunnel that draws air in from the surrounding room. All wind tunnel tests were conducted at a wind speed of nominally 44 m/s and using G-scale models, 1:29 scaled replica models of their full-scale counterparts. This resulted in Reynolds numbers based on the width of the models of 2.5×10^5. The air speed was measured using a pitot-probe and the freestream pressure and temperature were measured using the static pressure port from the pitot-probe and a thermocouple mounted near the top wall of the wind tunnel.

The train set considered in the wind tunnel consisted of a locomotive followed by five freight cars. The train set was mounted onto an elevated track system, as shown in the top image of Fig. 5. The simulated train bed was employed to allow space for the force measurement instrumentation and to aid in minimizing the influence of the boundary layer that exists along bottom of the wind tunnel. Each car in the train set was mounted using very thin wire to an individual track section that was instrumented with two commercial load cells as illustrated in the bottom panel of Fig. 5. Each section of the track was fabricated from aluminum channel and is instrumented with its own load cell system so that the drag on each of the individual cars could be measured. The load cells were carefully calibrated before every test using a weight and pulley system. This calibration was repeated at the end of every test, and in all cases the calibration results were essentially identical. The open section of the aluminum channel was filled with foam insert to fill the void space and better simulate the distance between railcars and the track. Further, a shield was placed at the front of the aluminum channel track to block

Fig. 5 Image of a train set in the wind tunnel (top) and a schematic of a track section, with accompanying load cells, on which one car from the train set was mounted (bottom)

any air flow from interacting with the load cells under each car. This track/train arrangement has been used to consider several different train scenarios, but for this present study the drag on only the leading locomotive is of interest.

In addition to a baseline configuration (no fairing), three fairings were tested, two from the primary fairing family and one from the secondary fairing family. The fairings were 3-D printed from a polymer material and sanded smooth. More specifics about the fairings tested will be given in the results section of the paper. Here we are only concerned about the drag on the leading locomotive. Each fairing configuration was tested at least four times and the results were averaged. Measurements of drag force, air temperature and pressure, and wind tunnel velocity were sampled at 1000 Hz and averaged over a 30 second interval for each test. All measurements were acquired by a National Instruments data acquisition (Model: SCXI - 1000) system. An average drag coefficient was then computed for each fairing scenario tested. Employing the propagation of error method, an uncertainty analysis was performed for all tests using the Student's t score based on a confidence interval of 95%. The total uncertainty measured drag coefficient values was ±0.85%. In the results section that follows, the wind tunnel results will be presented in terms of a drag reduction parameter that is defined below, which represents the deviation in the leading locomotive drag for the fairing cases compared to the baseline scenario.

3 Results

3.1 CFD drag reduction results

Drag reduction results for the 45 primary fairing geometries considered are plotted in Fig. 6. The dependent variable in the plots, D_R, is the normalized amount of drag reduction that occurs for each locomotive-fairing combination. It is defined as

$$D_R = \frac{D_B - D_F}{D_B}, \tag{6}$$

where D_B is the drag on the baseline (non-fairing) locomotive and D_F is the drag on the locomotive with a mounted fairing. Positive values of D_R indicate a drag reduction, whereas negative values indicate the fairing yields a drag increase. D_R is shown in Fig. 6 as a function of each of the design variables discussed previously. Three values of x_{1A} were explored: 61 cm, 122 cm, and 183 cm; and five values of x_{3A} were explored: 0 cm, 61 cm, 122 cm, 183 cm, and 244 cm. However, due to the linear constraint placed on the upper bound of x_{2A} (4), there was not a common set of values explored for x_{2A}. Instead, x_{2A} was normalized to form a new variable, $\overline{x_{2A}}$, defined by the expression

$$\overline{x_{2A}} = \frac{x_{2A}}{x_{2A,UB}}, \tag{7}$$

where $x_{2A,UB}$ is the local upper bound of x_{2A}. In this normalized form, a common set of three values of $\overline{x_{2A}}$ was explored: 0.0, 0.5, and 1.0.

The results for the primary fairing geometries were sorted into the three series that are shown on each of the three panels of Fig. 6, one for each value of x_{1A}. Each plot series is displayed in the legends of Fig. 6. Furthermore, each panel represents one of the three values of $\overline{x_{2A}}$ noted above. Finally, D_R is plotted as a function of x_{3A} on each panel.

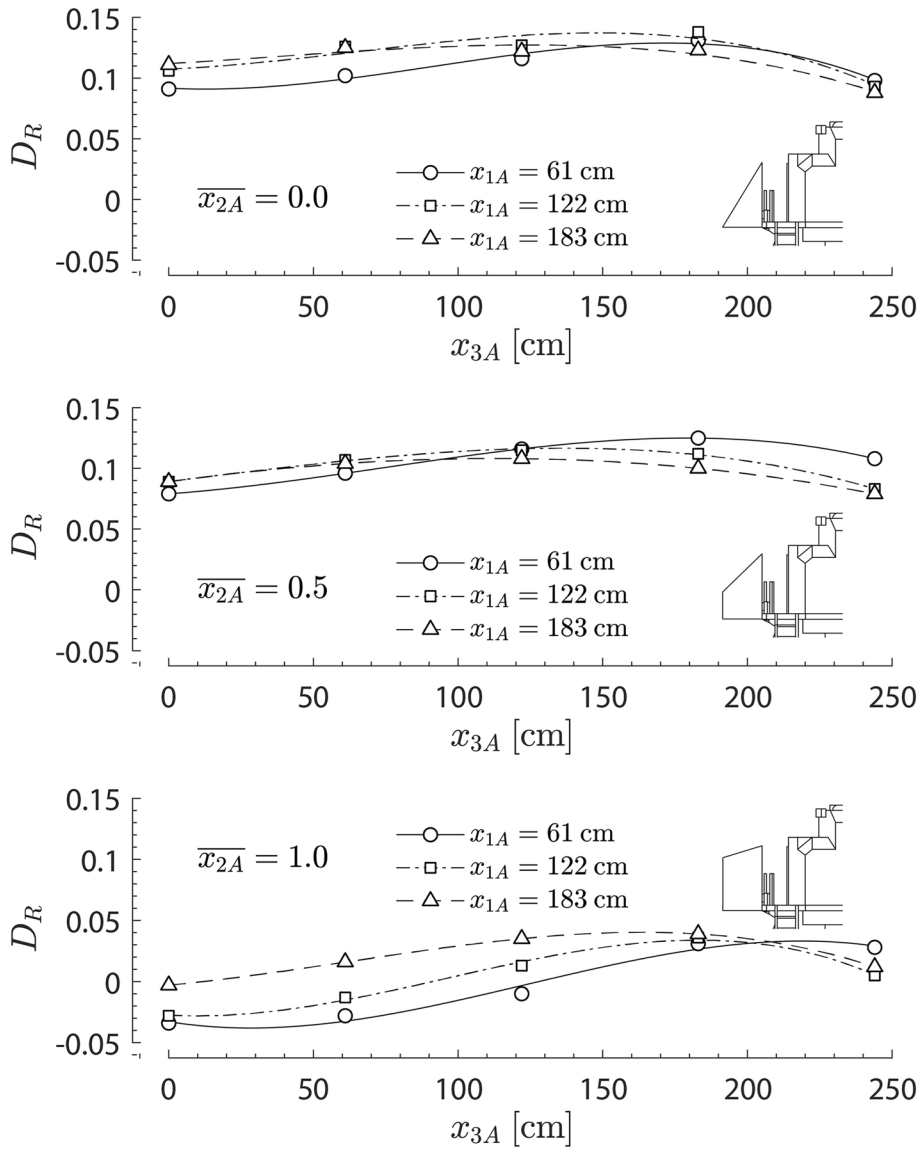

Fig. 6 Drag reduction (D_R) results for the primary fairing shape as a function of fairing length (x_{1A}), normalized tip height ($\overline{x_{2A}}$), and tip width (x_{3A})

The results of Fig. 6 reveal that D_R is more sensitive to $\overline{x_{2A}}$ than the other two variables, although all three variables exert influence on the drag reduction. With very few exceptions, D_R increases (less drag) as $\overline{x_{2A}}$ decreases (fairing tip height is moved lower). This observation is more evident as $\overline{x_{2A}}$ decreases from 1.0 to 0.5, where for fixed values of x_{1A} and x_{3A} the average decrease in D_R is approximately 0.1 (a nominal 10% rise in the locomotive drag).

In contrast to $\overline{x_{2A}}$, the effects of x_{1A} and x_{3A} on D_R are less systematic. For all scenarios considered, as the fairing tip width (x_{3A}) increases the drag reduction also increases up to a maximum amount, and after this point continuing to increase the tip width yields a decrease in D_R (increased drag). The value of x_{3A} where this happens also depends on the values of x_{1A} and $\overline{x_{2A}}$; however, the tip width where the drag reduction is the greatest

is almost always between 150 and 200 cm. With regard to the influence of x_{1A}, at values of x_{3A} lower than 150 cm, increases in the fairing length (x_{1A}) yield greater drag reduction. In contrast, when the fairing tip width is greater than 150 cm, increasing the fairing length yields less drag reduction.

The primary fairing shape that resulted in the largest drag reduction is defined by the following design variable values: $x_{1A} = 122$ cm, $\overline{x_{2A}} = 0.0$, and $x_{3A} = 183$ cm. The value of D_R for this scenario is 0.138, indicating that the total drag on the lead locomotive will be reduced by 13.8% when this fairing is deployed. An isometric rendering of this fairing is shown in the left panel of Fig. 7.

There are a few interesting findings from these results. First, although D_R is clearly not a monotonic function of x_{3A}, it very nearly is a monotonic increasing function of $\overline{x_{2A}}$. This may be a result of the fact that, due to the front window visibility constraint, the top of the fairing is further from the top of the locomotive than the sides of the fairing are from the sides of the locomotive. Thus, the top surface of the fairing must be steeper than the sides in order to compensate and direct the flow over the locomotive. Second, making the fairing more pointed by reducing the tip width results in increased drag. Indeed, in most scenarios for fixed values of x_{1A} and $\overline{x_{2A}}$, the worst performing fairings were those with the smallest tip width (the most pointed). When the fairing is made more pointed, it directs the incoming airflow too far beyond the sides of the locomotive. This is in contrast to the best performing fairing shown in the left panel of Fig. 7 which gently directs the flow around the sides of the locomotive. The penalty to D_R is especially high as the fairing becomes more pointed when the value of $\overline{x_{2A}}$ is 1.0. This observation suggests that by increasing the tip height of the pointed fairing, even more of the incoming airflow gets directed far beyond the sides of the locomotive, thus contributing to greater drag. Based on these observations, a second family of fairings was considered in which the primary fairing shape was modified in order to more effectively direct the incoming airflow over the top of the locomotive. This was accomplished by adding the sidewall features that resulted in the secondary fairing geometries.

Drag reduction values for the 15 secondary fairing geometries considered are presented in Fig. 8 as a function of the sidewall height (x_{1B}). Each of these 15 geometries had

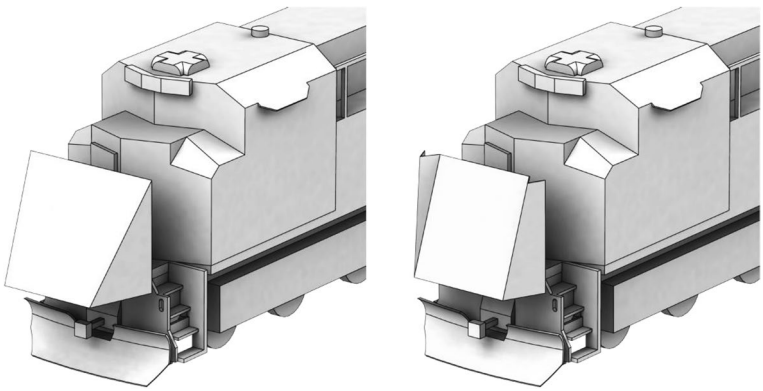

Fig. 7 Left Panel: Isometric rendering of the best performing geometry from the primary fairing shape family. The fairing is defined by the following design variable values: $x_{1A} = 122$ cm, $\overline{x_{2A}} = 0.0$, and $x_{3A} = 183$ cm. Right Panel: Isometric rendering of the best performing secondary fairing shape. The fairing is defined by the following design variables: $x_{1A} = 74$ cm, $\overline{x_{2A}} = 0.0$, $x_{3A} = 191$ cm, and $x_{1B} = 30$ cm

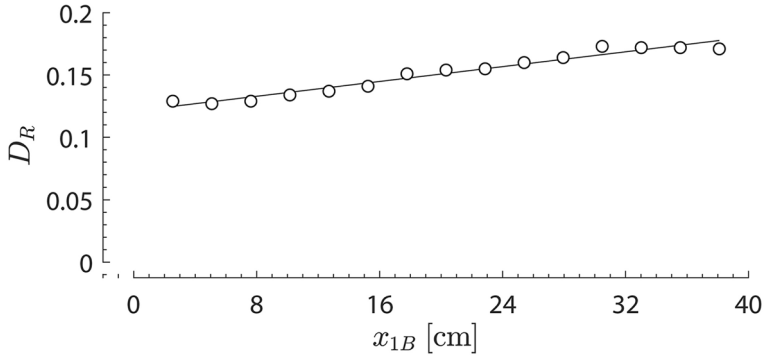

Fig. 8 Drag reduction (D_R) results for the secondary fairing shape as a function of side wall height (x_{1B}). Each secondary fairing geometry is defined by the following primary fairing shape variables: $x_{1A} = 74$ cm, $\overline{x_{2A}} = 0.0$, and $x_{3A} = 191$ cm

values of the other design variable values as follows: $x_{1A} = 74$ cm, $x_{2A} = 0$, and $x_{3A} = 191$ cm. The results show an approximately linear increase in D_R as x_{1B} is increased, up to $x_{1B} \approx 30$ cm. Beyond this value of side wall height, no further drag reduction was achieved. The best performing fairing from the secondary fairing shape yields a total drag reduction from the baseline locomotive of 17.3%. This represents a 25% greater reduction in drag relative to the best performing fairing from the primary family considered above. The sidewall height for this best case is $x_{1B} = 30$ cm, and an isometric rendering of this fairing is shown in the right panel of Fig. 7.

3.2 CFD flow field observations

We now turn attention to the manner in which the flow field and pressure distribution on the front of the locomotives are altered when fairings are added. Here we consider plots of the pressure coefficient on the front of the locomotive and attached fairings for three scenarios: 1. The baseline locomotive; 2. A locomotive with the best performing fairing from the primary fairing family; 3. A locomotive with the best performing faring from the secondary fairing family. Shown in Fig. 9 are plots of the pressure coefficient, C_P for the three scenarios, where C_P is defined as

$$C_P = \frac{P_S - P_\infty}{\frac{1}{2}\rho V_\infty^2}. \tag{8}$$

P_S is the local static pressure, P_∞ is the upstream pressure, ρ is the air density, and V_∞ is the freestream velocity.

The cumulative pressure drag on an object is directly influenced by the pressure distribution, and generally speaking, decreases in areas of stagnation yield an overall decrease in drag. Results from the simulations show that the pressure distributions on the rear side of the locomotives are essentially the same for all cases. Thus, differences in the pressure distributions on the front of the locomotive represent the primary mechanism for variations in drag for the different scenarios. In the contour plots of Fig. 9, blues and greens represent low values of C_P, yellows and oranges represent intermediate values, and reds correspond to high values of C_P.

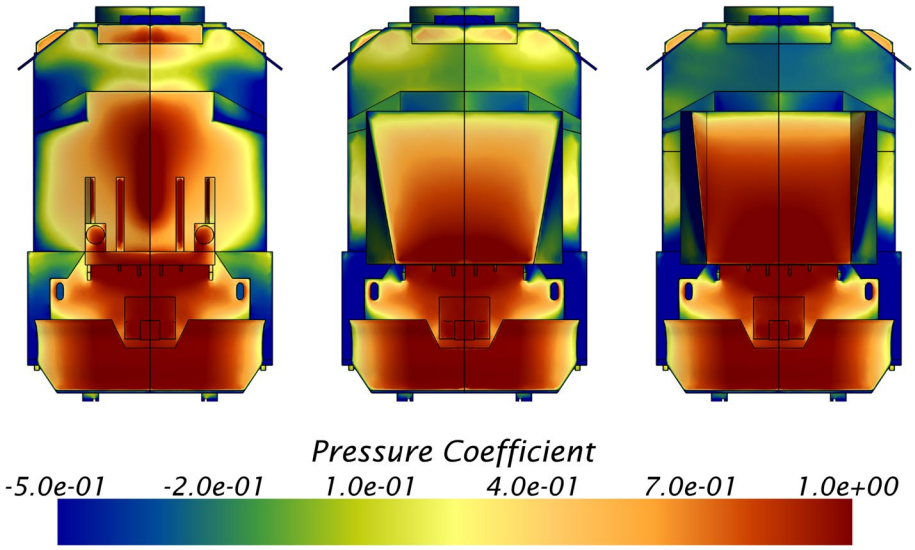

Fig. 9 Front-view surface plots of the static pressure coefficient, C_P, on the baseline locomotive without an add-on nose fairing (left), with the best performing primary fairing (middle), and with the best performing secondary fairing (right)

For all three scenarios of Fig. 9, the snow plow (bottom scoop surface) and the walkway platform (just below where the fairings are mounted) appear to have very similar C_P distributions and magnitudes. With regard to the baseline locomotive, the following behavior is evident: 1. $C_P \approx 1$ along the length of the four vertical stanchions and on the headlight and ditch light fixtures, and these are bluff shapes yielding large drag penalties; 2. A large vertical region of stagnation exists on the nose of the locomotive, with C_P decreasing moving sideways from the nose; 3. Above the nose of the locomotive and on the windshields, another strong stagnation zone exists. The best performing primary fairing covers the four vertical stanchions and ditch light fixtures and thus eliminates them as drag sources. It further yields a notable decrease in the size and magnitude of the stagnation that occurs near the windshields. The most notable difference in the C_P distributions between the best performing primary and secondary fairings is that there is actually a larger region of high C_P on the secondary fairing. However, this is accompanied by much lower values of C_P on the cab of the locomotive above the tops of the fairings and in the region surrounding the windshields.

To supplement the C_P surface plots of Fig. 9, streamline plots are provided in Fig. 10 that further reveal and confirm the anticipated effect of adding side walls. The streamlines were generated for the secondary fairing shapes with 0 and 30 cm sidewalls. The streamline seeds come from a uniform grid of coordinates about five centimeters upstream of the front face of the fairing. The streamlines are colored by the normalized magnitude of the total fluid velocity (normalization by the freestream velocity). As is shown in the figure, the airflow stagnates on the middle of both fairings and accelerates around the corners of them. However, when the side walls are present, the lateral component of the flow is smaller due to local stagnation on the side walls, and the resulting pressure gradient bends the streamlines upwards. As a result, the vertical moving flow toward the top of the locomotive is energized to a

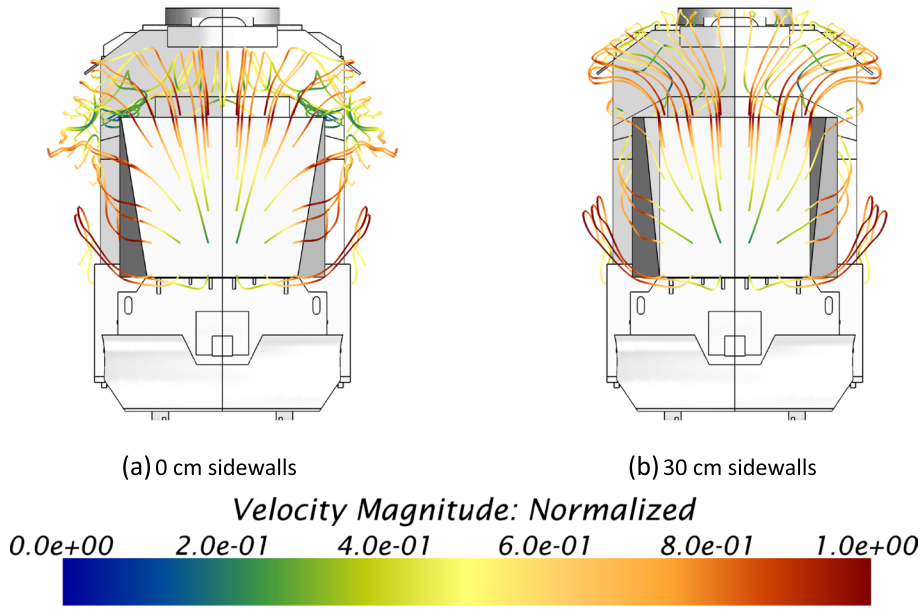

Fig. 10 Streamlines colored by the ratio of local velocity magnitude to freestream velocity magnitude for two secondary fairing geometries as seen from in front of the train: (a) 0 cm sidewalls and (b) 30 cm sidewalls

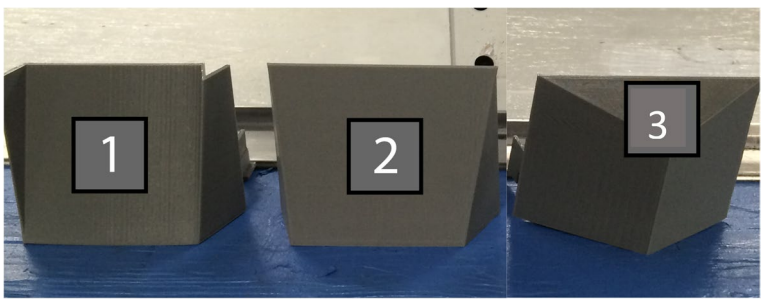

Fig. 11 Image of three fairings tested in the wind tunnel experiments

greater extent. When the sidewalls are not present (panel (a)), local stagnation on the front windows occurs. This stagnation causes a local region of swirling flow with a significant fraction of the air being redirected to move around the sides of the locomotive. In contrast, when the sidewalls are present (panel (b)), the recirculation zone near the windshields is completely eliminated, the increasingly energized streamlines bend smoothly over the top of the locomotive, and the amount of stagnation is greatly reduced.

3.3 Wind tunnel results

Wind tunnel tests were conducted for the three fairings that are shown in Fig. 11, two from the primary fairing family (numbers 2-3) and one from the secondary fairing family (number 1). Table 1 provides the values of x_{1A}, $\overline{x_{2A}}$, and x_{3A} that the fairings would have if they were full-scale (rather than 29th scale models). None of the five geometries were tested in the CFD model; however, Stucki [34] produced a second order multidimensional polynomial regression model for each family that can be used to predict D_R for

Table 1 Drag reduction and design variable values for the five fairings tested in the wind tunnel. Dimensioned variables are given in cm

Fairing #	D_R (CFD)	D_R (Exp.)	x_{1A}	$\overline{x_{2A}}$	x_{3A}	x_{1B}
1	0.16	0.11	70	0	194	38
2	0.12	0.08	70	0	194	0
3	0.02	−0.04	70	0.797	0	0

each of the five fairing geometries. The regression model for the primary fairing family was produced from CFD data from 90 primary fairing geometries, and the regression model for the secondary fairing family was produced from CFD data from 50 secondary fairing geometries. Table 1 provides the value of D_R obtained for each fairing from both the wind tunnel tests and the CFD-based regression models. Recall that the CFD simulations considered two in-line locomotives, while the wind tunnel testing considered a single locomotive with five trailing freight cars. Also, the CFD simulations were conducted at a Reynolds number of 4.4×10^6 and the experiments were conducted at $Re = 2.5 \times 10^5$. Furthermore, the CFD analysis considered geometries that due to practicality could not include all of the detailed features that exist on a production locomotive. In contrast, the physical model used in the wind tunnel was made by a professional model builder and includes many more features than the CFD model. Lastly, in the CFD model the ground was allowed to translate with the approaching air stream, consistent with the dynamics of a train moving down a track. In the wind tunnel testing the track and ground remained stationary, although this affect is likely a minor contributor. Because of all four of the above noted important differences, it was expected that there will be differences in the amounts of drag reduction that exist in the CFD and testing results. Here we are interested in comparing the overall trends between the CFD and wind tunnel results.

The wind tunnel results show consistent trends with the CFD data described above, although the amount of drag reduction observed in the experiments is generally less than that predicted by the CFD modeling. The deviation in the results could be attributed to the differences noted above. Addition of sidewalls on the fairings increases D_R for both the experimental and CFD cases. This is evident by comparing D_R for fairing numbers 1 and 2. Further, increasing the tip height ($\overline{x_{2A}}$) and decreasing the tip width (x_{3A}) leads to greater drag for both the CFD simulations and the wind tunnel experiments. When the tip height is located at the top of the faring versus the bottom of the fairing, both the CFD and experimental data predict a drag increase of nearly the same amount.

4 Conclusions

This paper presents CFD results from a design study that considers add-on nose fairings for reducing drag on lead locomotives in freight trains. The study consists of 45 fairing geometries from a primary fairing shape and 15 fairing geometries from a secondary fairing shape. The primary fairing is shaped like a wedge, and the secondary fairing is shaped like a wedge with sidewall features. The designs for both fairing shapes consist of flat planar panels in order to enable a foldable origami construction to allow deployment when in use and to be stowed when not in use. The best performing of the 45 primary

fairing geometries reduced drag on the lead locomotive by 13.8%. Adding side wall features also proved to be effective at reducing drag, and the best performing of the 15 secondary fairing geometries reduced drag on the lead locomotive by 17.3%.

Qualitative analysis of the flow field confirmed that the sidewall features of the secondary fairing geometry aided in directing the incoming airflow over the top of the locomotive. Without the sidewall features, the flow was shown to stagnate on the locomotive front windows beneath the headlight fixtures, thus developing a large region of recirculating flow. Results from wind tunnel tests on three of the fairings considered in the CFD study reveal behavior that is consistent with the CFD results; however, the magnitudes of observed drag reductions were smaller in the experimental testing.

Acknowledgements
Not applicable.

Authors' contributions
Both authors contributed equally to the manuscript. The authors read and approved the final manuscript.

Funding
Not applicable.

Availability of data and materials
All data in the manuscript will be made available through request to the corresponding author.

Declarations

Competing interests
The authors do not have any financial or non-financial interests directly or indirectly related to this work.

Received: 17 June 2022 Accepted: 22 October 2022
Published online: 02 December 2022

References

1. Hu PS, Schmitt R, Sprung MJ et al (2017) National Transportation Statistics. U.S. Department of Transportation, Washington DC. https://www.bts.gov/national-transportation-statistics-2017-4th-quarter
2. Golovanevskiy VA, Chmovzh VV, Girka YV (2012) On the optimal model configuration for aerodynamic modeling of open cargo railway train. J Wind Eng Ind Aerodyn 107–108:131–139
3. Paul JC, Johnson RW, Yates RG (2009) Application of CFD to rail Car and locomotive aerodynamics. In: Browand F, McCallen R, Ross J (eds) The aerodynamics of heavy vehicles II: trucks, buses, and trains. Springer, Berlin, Heidelberg, pp 259–297
4. Dayman B (1983) Demonstration of the coast-down technique for determining train resistances. NASA Contr Rep NASA-CR-173468
5. Pan D, Zhao L, Luo Q et al (2018) Study on the performance improvement of urban rail transit system. Energy. 161:1154–1171
6. Roshko A (1961) Experiments on the flow past a circular cylinder at very high Reynolds number. J Fluid Mech 10(3):354–356
7. Östh J, Krajnović S (2014) A study of the aerodynamics of a generic container freight wagon using large-eddy simulation. J Fluids Struct 44:31–51
8. Watkins S, Saunders JW, Kumar H (1992) Aerodynamic drag reduction of goods trains. J Wind Eng Ind Aerodyn 40(2):147–178
9. Condie R, Maynes D (2014) Methods for reducing aerodynamic drag on cargo carrying railcars. In: Proceedings of the ASME 2014 4th joint US-European fluids engineering division summer meeting collocated with the ASME 2014 12th international conference on nanochannels, microchannels, and minichannels, Chicago, August 3–7, 2014
10. Kinghorn PD (2017) Aerodynamic drag on intermodal rail cars. Thesis, Brigham Young University
11. Lai YC, Barkan CPL (2005) Options for improving the energy efficiency of intermodal freight trains. J Transp Res Board 1916:47–55
12. Choi H, Lee J, Park H (2014) Aerodynamics of heavy vehicles. Annu Rev Fluid Mech 46:441–468
13. Salati L, Schito P, Cheli F (2017) Wind tunnel experiment on a heavy truck equipped with front-rear trailer device. J Wind Eng Ind Aerodyn 171:101–109
14. Kim JJ, Lee S, Kim M et al (2017) Salient drag reduction of a heavy vehicle using modified cab-roof fairings. J Wind Eng Ind Aerodyn 164:138–151
15. kim JJ, Hong J, Lee SJ (2017) Bio-inspired cab-roof fairing of heavy vehicles for enhancing drag reduction and driving stability. Int J Mech Sci 131-132:868–879
16. Malviya V, Mishra R, Fieldhouse J (2009) CFD investigation of a novel fuel-saving device for articulated tractor-trailer combinations. Eng Appl Comp Fluid Mech 3(4):587–607

17. Chowdhury H, Moria H, Ali A et al (2013) A study on aerodynamic drag of a semi-trailer truck. Procedia Eng 56:201–205
18. Schetz JA (2001) Aerodynamics of high-speed trains. Annu Rev Fluid Mech 33:371–414
19. Baker C (2010) The flow around high speed trains. J Wind Eng Ind Aeroyn 98:277–298
20. Liu T, Chen Z, Zhou X (2018) A CFD analysis of the aerodynamics of a high-speed train passing through a windbreak transition under crosswind. Eng Appl Comp Fluid Mech 12(1):137–151
21. Niu J, Wang Y, Zhou D (2019) Effect of the outer windshield schemes on aerodynamic characteristics around the car-connecting parts and train aerodynamic performance. Mech Syst Signal Process 130:1–16
22. Tschepe J, Fischer D, Nayeri CN et al (2019) Investigation of high-speed train drag with towing tank experiments and CFD. Flow Turbulence Combust 102:417–434
23. Lee Y, Kim KH, Rho JH et al (2016) Investigation on aerodynamic drag of Korean high speed train (HEMU-430X) due to roof apparatus for electrical device. J Mech Sci Technol 30:1611–1616
24. Kwak M, Yun S, Lee Y et al (2013) Optimum nose shape of a front-rear symmetric train for the reduction of the total aerodynamic drag. J Mech Sci Technol 27:3733–3743
25. Li X, Chen G, Zhou D et al (2019) Impact of different nose lengths on flow-field structure around a high-speed train. Appl Sci 9(21):4573
26. Li M, Liu B, Liu TH et al (2020) Improved delayed detached eddy simulation of the slipstream and trackside pressure of trains with different horizontal profiles. J App Fluid Mech 13(2):457–468
27. Wu Z, Xie Z, Wang P et al (2020) Aerodynamic drag performance analysis of different types of high-speed train pantograph fairing. J App Sci Eng 23(3):509–519
28. Hemida H, Krajnović S (2010) LES study of the influence of the nose shape and yaw angles on flow structures around trains. J Wind Eng Ind Aerodyn 98(1):34–46
29. Iden ME (2015) Drag reducing devices for a locomotive. US Patent US9085306B2, 21 Jul 2015
30. Seymour K, Burrow D, Avila A et al (2018) Origami-based deployable ballistic barrier. In: Proceedings of the 7th international meeting on origami in science, mathematics and education, Oxford, 5-7 September 2018, pp 763–778
31. Zirbel SA, Lang RJ, Thomson MW et al (2013) Accommodating thickness in origami-based deployable arrays. J Mech Des 135(11):111005
32. Kuribayashi K, Tsuchiya K, You Z et al (2006) Self-deployable origami stent grafts as a biomedical application of Ni-rich TiNi shape memory alloy foil. Mat Sci Eng A 419:131–137
33. Tolman KA, Crampton EB, Stucki C et al (2018) Design of an origami-inspired deployable aerodynamic locomotive fairing. In: Proceedings of the 7th international meeting on origami in science, mathematics and education, Oxford, 5-7 September 2018, pp 669–684
34. Stucki CL (2019) Aerodynamic design optimization of a locomotive nose fairing for reducing drag. Thesis, Brigham Young University
35. Versteeg HK, Malalasekera W (2007) An introduction to computational fluid dynamics: the finite volume method, 2nd edn. Pearson, NY

Publisher's Note